Int. J. Electrochem. Sci., 16 **(2021)** 150951, doi: 10.20964/2021.01.08

International Journal of
ELECTROCHEMICAL
SCIENCE
www.electrochemsci.org

High-performance Photoelectrocatalytic Reduction of CO_2 by the hydrophilic–hydrophobic composite Cu-SnO_2/ZIF-8

Dingding Zhang, Huimin Yang [*], Yupeng Li, Zhifang Li, Nan Gao, Wenjing Zhou, Zhenhai Liang [*]

College of Chemistry & Chemical Engineering, Taiyuan University of Technology, Taiyuan 030024, PR China
[*]E-mail: yanghuimin@tyut.edu.cn (Huimin Yang), liangzhenh@sina.com (Zhenhai Liang)

Received: 2 September 2020 / *Accepted:* 28 October 2020 / *Published:* 30 November 2020

Photoelectrocatalytic reduction CO_2 can solve energy shortages and environmental problems. However, the poor solubility and intense competition of the hydrogen evolution reaction (HER) seriously restrict CO_2 activation. Here, a hydrophilic–hydrophobic Cu-SnO_2/ZIF-8 composite catalyst was constructed by compounding hydrophobic ZIF-8 with hydrophilic Cu-SnO_2. Gas-phase CO_2 was directly used to improve the activation efficiency of CO_2 molecules, and hydrogen evolution was inhibited. Results showed that when the overpotential was as low as ~364 mV, the Faraday efficiency of formic acid reached 68.96%. The maximum current density approached 12.8 mA·cm^{-2} at -1.4V versus the Ag/AgCl electrode. The ZIF-8 unique structure promoted electron transfer and Cu-SnO_2 dispersion to provide additional active sites. The excellent photocatalytic performance of Cu-SnO_2/ZIF-8 may be attributed to the special hydrophilic–hydrophobic structure and the small band gap that can absorb much visible light.

Keywords: Hydrophilic-hydrophobic structure, CO_2 reduction, Photoelectrocatalysis, ZIF-8, Sn-based nanoparticles

1. INTRODUCTION

The conversion of CO_2 into gaseous fuels or high-energy liquids is a promising way to store energy and solve energy shortages and environmental problems [1]. However, practical implementation is difficult to achieve due to the chemical inertness of CO_2 and the multiple electron and proton transfer involved in converting CO_2 to numerous products. An effective and economical way to transform CO_2 into valuable products is an effective strategy[2]. CO_2 photoelectrocatalytic reduction combines the advantages of electrocatalysis and photocatalysis [3] and is the most promising method that utilizes sunlight with only mild reaction conditions. However, the poor solubility, slow diffusion rate, and intense competition of hydrogen evolution reaction (HER) seriously restrict the activation efficiency of CO_2 in the photoelectric catalytic system. Many methods, including ion doping[4] and introduction of

co-catalysts [5], have been proposed to improve the catalytic activity of the catalyst. However, the supply of CO_2 is another key factor that is always overlooked. When water is used as the proton source, traditional catalysts can only use a small amount dissolved CO_2 and cannot use most of the gas-phase CO_2. A catalyst with a hydrophilic–hydrophobic structure can effectively solve this problem. The hydrophobic layer can directly transport CO_2 gas to the reaction system to inhibit the competitive HER, and the hydrophilic layer can provide protons for the reaction to effectively promote CO_2 reduction.

A hydrophobic zeolite imidazolate framework (ZIF-8) layer is introduced on the surface of the photocatalyst to suppress the competitive HER and enhance the interaction between CO_2 and catalyst, thus improving the efficiency and selectivity of CO_2 reduction [6]. ZIF-8 with zeolite-like structure is an important branch of Metallic Organic Framework (MOF) with excellent CO_2 adsorption performance, a considerable specific surface area, and abundant rich pyridine N and has been extensively applied as an ideal photoelectrocatalyst[7]. Wang et al.[8] studied the effects of different zinc sources on the structures and properties of ZIF-8, and the ZIF-8 prepared using $ZnSO_4$ exhibited the highest CO_2 catalytic performance with a CO yield of 65%. Further research showed that the discrete Zn node in ZIF-8 may act as the active sites. Liu et al.[9] successfully synthesized Zn_2GeO_4/ZIF-8 nanorods that showed excellent performance in the photocatalytic conversion of CO_2 to methanol because ZIF-8 can capture CO_2 from water and improve the photocatalytic activity of Zn_2GeO_4.

The limited conductivity and light absorption capacity of pure ZIF-8 severely limit its application in electrocatalysis and photocatalysis [10]. As a solution, ZIF-8 can be combined with hydrophilic semiconductor materials to construct a hydrophilic–hydrophobic structure and effectively improve the photoelectric properties of ZIF-8. SnO_2 is an important wideband gap N type semiconductor (Eg=3.62 eV) with good catalytic, gas sensitivity, and special photoelectric properties[11]. Zhang et al.[12] loaded SnO_2 nanoparticles onto carbon cloth and successfully reduced CO_2 into formate with Faraday efficiency (FE) of as high as 89% and overpotential of 0.88V, indicating that SnO_2 can facilitate the photoelectrocatalytic reduction of CO_2 and shows excellent formate selectivity. In addition, the impurity level introduced by doping metal or non-metal ions can reduce the incident photon energy required by SnO_2 and inhibit the recombination of photons and holes. Hu et al.[13] used a one-step hydrothermal method to prepare Cu-doped SnO_2 for photoelectrocatalytic CO_2 reduction, and the FE of formate was 12 times higher than that of pure SnO_2.

In this work, Cu-SnO_2 and ZIF-8 were combined to construct a hydrophilic–hydrophobic catalyst to convert CO_2 to formic acid under the synergy of photoelectricity. The hydrophilic SnO_2 modified by Cu ion doping is the catalytic active center that selectively generates formate under low overpotential. The hydrophobic ZIF-8 can directly capture bubbles in the electrolyte when in contact with the liquid, and the porous structure adsorbs a large number of CO_2 molecules, thereby achieving the coexistence of gas, liquid, and solid phases at the nanometer level. This three-phase interface structure can directly transfer CO_2 from the gas phase to the photoelectric catalytic reaction interface[6], thus allowing CO_2 to effectively capture electrons and improving the photoelectric catalytic efficiency. As a carrier, ZIF-8 with a porous structure has good atomic hydrogen storage and transfer properties[14] and can rapidly transfer the H atoms generated in the hydrophilic layer to prevent H_2 formation.

2. EXPERIMENTAL SECTION

2.1 The synthesis of ZIF-8 and Cu-SnO_2/ZIF-8 Nanostructures

The prototypical synthesis of ZIF-8 is as follows: Solution A was formed by dissolving 1.4700 g of $Zn(NO_3)_2$•$6H_2O$ in 100 mL of methanol, and solution B was generated by dissolving 3.2542 g of 2-methylimidazole in 100 mL of methanol with stirring. Solution A was added into solution B with vigorous stirring for 30 min, and the mixture was aged at room temperature for 24 h. The solid product named as ZIF-8 was separated through centrifugation, washed subsequently with methanol for three times, and finally dried at 60 °C for 10 h.

The Cu-SnO_2/ZIF-8 composite was prepared by simple in-situ synthesis. Cu-SnO_2 was synthesized with $SnCl_4 \cdot 5H_2O$ as the precursor and anhydrous $CuCl_2$ as the dopant in accordance with the method of Hu et al. [12], followed by the in situ growth of ZIF-8 nanoparticles synthesized on Cu-SnO_2 nanospore structures. According to the molar ratio of ZIF-8 to Cu-SnO_2, the catalyst was named as 1:x-Cu-SnO_2/ZIF-8.

2.2 Catalyst Characterization

The crystal structure was characterized by X-ray diffraction (XRD, Siemens DX-2007 diffractometer, 40kV, Cu Kα). Scanning electron microscopy (SEM) was performed on a JEM-2010 FESEM to detect the morphologic details and sizes of the prepared samples. Transmission electron microscopy (TEM) and high-resolution transmission electron microscopy (HRTEM) images were used to identify the morphology, size, and nanocrystalline structure of the sample (Tecnai G2 F20S-Twin). The specific surface area of Bruna- Emmett-Teller (BET) of the catalyst was analyzed by nitrogen adsorption on the Micromeritics ASAP 2020 nitrogen adsorption device. X-ray photoelectron electron spectroscopy (XPS) was conducted on a Thermo Fisher ESCALAB 250 xi photoelectron spectroscopy to obtain the information of element composition and content, chemical state, molecular structure and chemical bond of the catalyst.

2.3 Photoelectrochemical Measurements

Cyclic voltammetry (CV), Linear scan volt-ampere (LSV), electrochemical impedance spectroscopy (EIS), Tafel and transient photocurrent response measurements were performed in a three-electrode H-type cell using PLS-LXE 300 xenon lamps and electrochemical workstations (Princeton Versastat 3). 1H NMR spectrum was used to qualitatively and quantitatively analyze the liquid products.

2.4 Calculations

① All potentials reported in this paper are rescaled to reversible hydrogen electrode (RHE) according to Eq. (1).

$$E(\mathrm{RHE}) = \mathrm{E(Ag/AgCl)} + 0.197 + 0.059 \times \mathrm{pH} \quad (1)$$

② The RHE for CO_2 reduction to HCOOH.

$$CO_2 + 2H^+ + 2e^- = HCOOH, E^{\theta'} = -0.2\,V(vs.RHE) \quad (2)$$

③ The band gap value can be obtained by Kubelka-Munk theorem.

$$(\alpha h\nu)^{1/n} = A(h\nu - Eg) \quad (3)$$

Where α represents the light absorption coefficient, h is the Planck constant, ν represents the frequency of illumination, A is a proportional constant, and n is determined by the transition mode of the semiconductor.

④ The tafel parameter can be calculated according to Eq (4).

$$\eta = a + b \cdot \log|i| \quad (4)$$

where η represents overpotential; a and b are constant; i is current density ($A \cdot cm^{-2}$);

⑤ The electrode reaction mechanism and speed control steps are determined according to Butler-Volmer equation, the Eq (5).

$$j = j_0 \cdot \left\{ \exp\left[\frac{\alpha_a zF}{RT}(E - E_{eq}) \right] - \exp\left[-\frac{\alpha_c zF}{RT}(E - E_{eq}) \right] \right\} \quad (5)$$

where α_a and α_c are the dimensionless anodic and cathodic charge transfer coefficients, respectively, z is the number of electrons, F is the Faraday constant, R is the universal gas constant, and T is temperature (293.15 K); j_0 is exchange current density ($A \cdot cm^{-2}$).

⑥ According to the element electronegativity theory, the positions of the bottom of the semiconductor band (E_{CB}) and the top of the valence band (E_{VB}) can be calculated. The calculation formula is as follows:

$$E_{CB} = -[\chi(A)^a \cdot \chi(B)^b]^{1/(a+b)} + E_0 + 0.5E_g \quad (6)$$

$$E_{VB} = E_{CB} + E_g \quad (7)$$

where $\chi(A)$ and $\chi(B)$ are the electronegativity of elements A and B, E_g is the band gap width, and E_0 is the reduction potential of water (4.5 eV).

⑦ The faradaic efficiency can be calculated by Eq (8).

$$FE_{HCOO^-} = \frac{zFn_{HCOO^-}}{Q} \quad (8)$$

where n_{HCOO^-} is the molar amount of formate produced; z is the number of transferred electron to form formate (z is 2 here); F is the Faraday constant, 96485 $C \cdot mol^{-1}$; Q is the total electrons passed the electrode within 1 h reaction.

3. RESULTS AND DISCUSSION

3.1. Catalytic Physicochemical Characterization

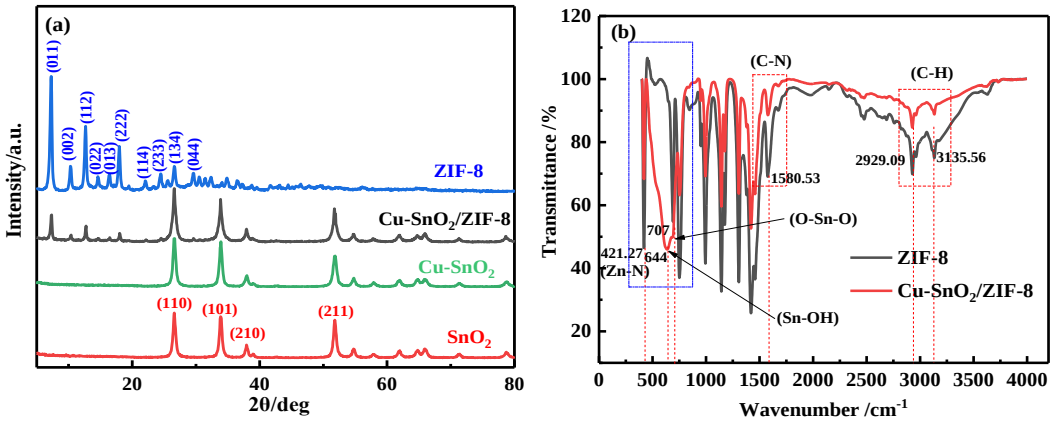

Figure 1. (a) XRD pattern of ZIF-8, Cu-SnO_2 and Cu-SnO_2/ZIF-8; (b) FT-IR spectrum of ZIF-8 and Cu-SnO_2/ZIF-8.

The XRD patterns of SnO_2, Cu-SnO_2, ZIF-8, and Cu-SnO_2/ZIF-8 are shown in Fig.1a. The diffraction peaks at 2θ=26.62°, 33.90°, 51.79° of Cu-SnO_2 correspond to the (110), (101), and (211) crystal faces of the rutile structure SnO_2[15], respectively, implying that SnO_2 still maintains a complete crystal structure after Cu ion doping. Primary diffraction peaks at 7.4°, 10.4°, 12.7°, 14.7°, 16.4°, 18.0°, 22.1°, 24.5°, 26.7°, and 29.6° correspond to the (011), (002), (112), (022), (013), (222), (114), (233), (134) and (044) of ZIF-8, thus confirming the typical sodalite structure of ZIF-8[16–18]. The characteristic peaks of Cu-SnO_2 and ZIF-8 can be clearly seen in the XRD pattern of Cu-SnO_2/ZIF-8, indicating that Cu-SnO_2 and ZIF-8 were successfully compounded while the crystal lattice structure of ZIF-8 was maintained. The electron density of ZIF-8 nanospheres was changed due to their combination with Cu-SnO_2, resulting in a decrease in the relative strength of the low Miller index surface (011)[19]. This finding further illustrates the formation of Cu-SnO_2/ZIF-8.

FTIR spectra (Fig.1b) proved the successful preparation of Cu-SnO_2/ZIF-8 complex. The absorption peaks at 3335.56 and 2929.09 cm^{-1} in ZIF-8 belong to the stretching vibration peaks of the C-H bond in the methyl and imidazole rings, respectively. The C=N bond stretching vibration peak on the imidazole ring at 1580.53 cm^{-1} and the stretching vibration peak of Zn-N at 421.27 cm^{-1} confirmed the chemical combination of zinc ions with the nitrogen atoms of methylimidazole groups[20]. The absorption peaks belonging to the NH...N hydrogen bond and the vibration peak of the N-H bond in 2-methylimidazole did not appear at 2600 and 1483 cm^{-1}, indicating that the dimethylimidazole can be completely deprotonated in the synthesis system[21,22]. The synthesized ZIF-8 was pure phase ZIF-8. Compared with ZIF-8, the Cu-SnO_2/ZIF-8 exhibit vibration peaks at 644 and 707 cm^{-1} due to the stretching vibration of the Sn-OH functional group and the bridge oxygen bond in the O-Sn-O functional group[23]. The peak strength was slightly lower than ZIF-8, indicating that the introduction of Cu-SnO_2 had reduced ZIF-8 bond energy, and Cu-SnO_2 successfully entered and interacted with ZIF-8.

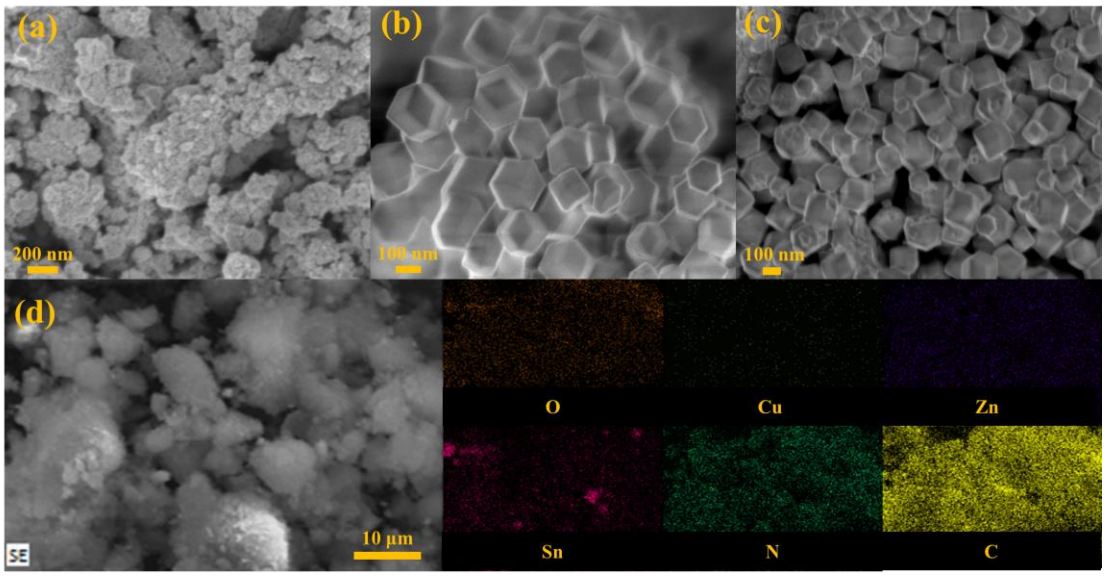

Figure 2. SEM images of Cu-SnO_2(a), ZIF-8(b) and Cu-SnO_2/ZIF-8(c) catalyst and the EDS of Cu-SnO_2/ZIF-8(d)

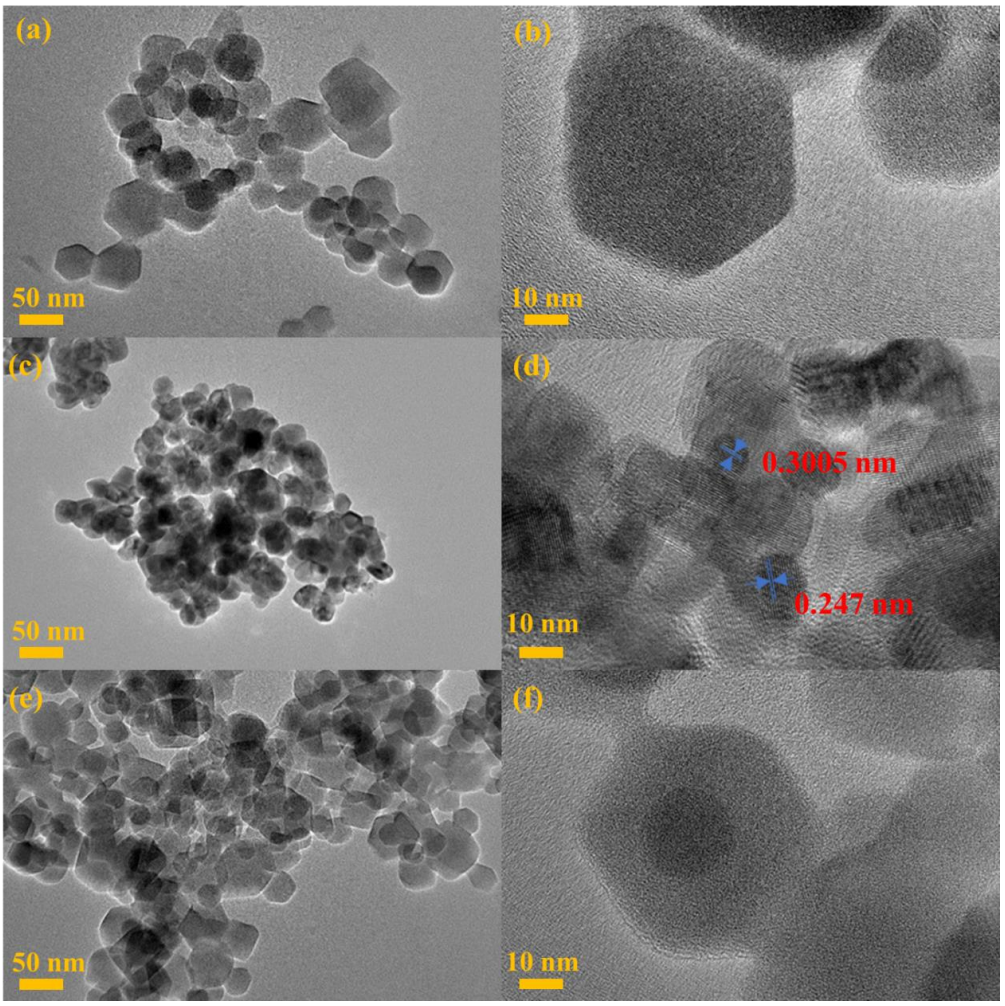

Figure 3. TEM images of pure ZIF-8(a-b), Cu-SnO_2(c-d) and Cu-SnO_2/ZIF-8(e-f)

SEM results revealed that Cu-SnO_2 is an agglomerate formed by spherical particles, and ZIF-8 has a rhombic dodecahedral shape with relatively uniform size. Cu-SnO_2/ZIF-8 has better dispersion than pure ZIF-8 and maintains the size and uniform rhombic dodecahedral structure of the latter. The Cu-SnO_2 nanospheres dispersed on ZIF-8 surface, which substantially reduced the agglomeration of Cu-SnO_2 nanoparticles and exposed additional catalytically active sites. Figure 2d shows the EDS diagram of Cu-SnO_2/ZIF-8. C, Zn, N, Sn, Cu, and O elements were uniformly distributed throughout the composite.

Pure ZIF-8 nanoparticles are rhombic dodecahedral structure with a diameter of 100 nm as shown in Figs.3a–b. Figure 3c displays that the SnO_2 after Cu doping are spherical and uniform in shape with particle size of approximately 20 nm. High-magnification image of Cu-SnO_2 reveals the interplanar distances of 0.247 and 0.305 nm in Fig.3d correspond to the (110) and (101) planes of SnO_2, respectively. The lattice spacing was changed slightly compared with that of pure SnO_2[24], due to the effect of Cu on the lattice and crystal morphology of SnO_2. As shown in Fig.3e, the Cu-SnO_2/ZIF-8 complex is evenly dispersed, and ZIF-8 can effectively alleviate the slight agglomeration of Cu-SnO_2 nanoparticles. Figure 3f reveals that spherical Cu-SnO_2 nanoparticles adhered to the surface of ZIF-8, thereby verifying the successful combination of Cu-SnO_2 and ZIF-8.

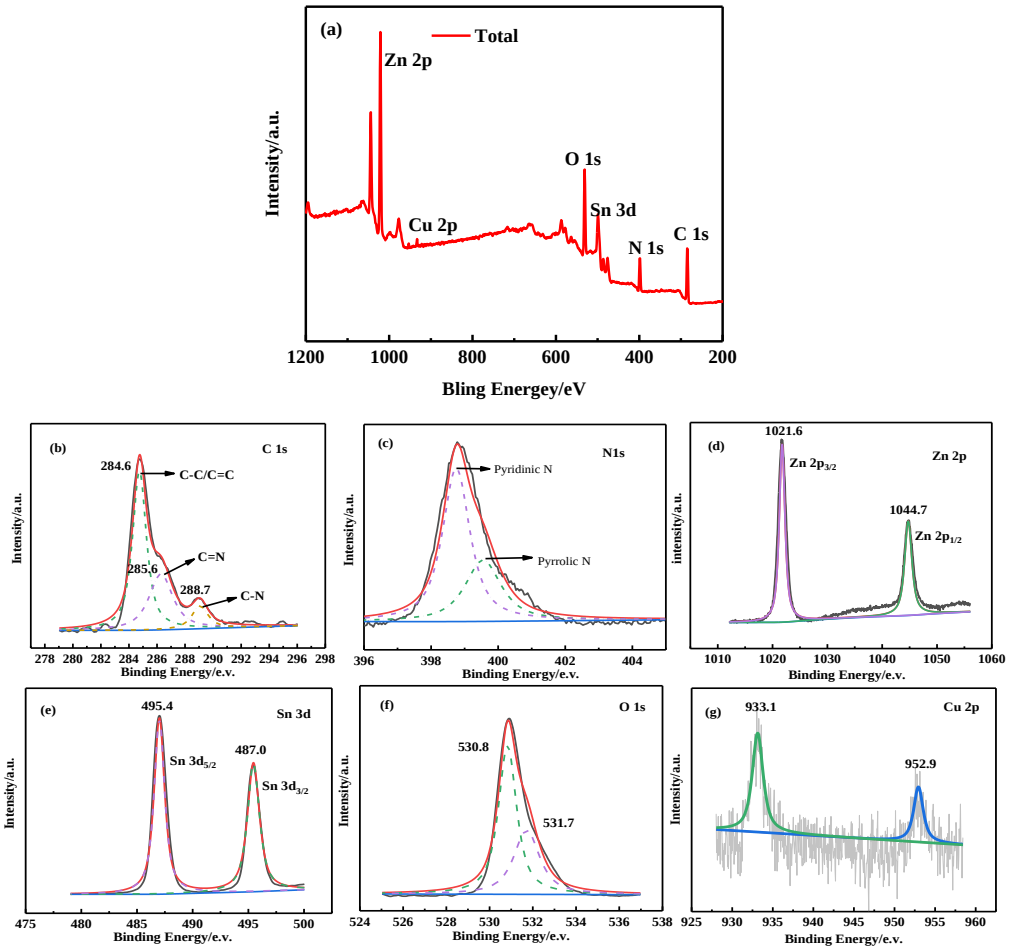

Figure 4. The 1:4-Cu-SnO_2/ZIF-8 XPS spectrum, (a) total; (b) C 1s; (c) N 1s; (d) Zn 2p; (e) Sn 3d; (f) O 1s; (g) Cu 2p.

Zn, C, N, Sn, O, and Cu elements can be observed from the full spectrum of XPS (Fig.4a). Figure 4b shows the fine spectrum of C 1s that can be divided into three peaks at 284.6, 284.6, and 288.7 eV attributed to C-C/C=C, C=N, and C-N, respectively[25]. The fine spectrum of N 1s is divided into two peaks at 398.5 and 400.0 eV corresponding to pyridine-type nitrogen and pyrrole-type nitrogen, respectively. Both can improve the surface adsorption effect of the catalyst on CO_2. Pyridine-type nitrogen atom is the active site of electrochemical reduction of CO_2[26,27]. The fine spectrum of Zn 2p with two peaks at 1044.7 and 1021.6 eV confirmed the presence of Zn^{2+}[28], which can act as Lewis acidic sites [29]. The Sn $3d_{3/2}$ and Sn $3d_{5/2}$ at 495.4 and 487.0 eV in Fig.4e indicates that the Sn in this material exhibits +4 valence [30]. The two asymmetric peaks at 530.8 and 531.7 eV in Fig.4f correspond to the two states of oxygen, namely, lattice oxygen and oxygen vacancy, respectively. Oxygen vacancy, an important active site for CO_2 reduction, can further enhance the photoelectricity performance of catalysts[31]. The Cu $2p_{3/2}$ and Cu $2p_{1/2}$ at 933.1 and 952.9 eV in Fig. 4g imply that the Cu particles were doped into the interior of the SnO_2 lattice with +2 valence. The difference in electronegativity between Cu and Sn inevitably leads to the transfer of valence electrons, thus causing SnO_2 lattice defects and oxygen vacancy formation[32].

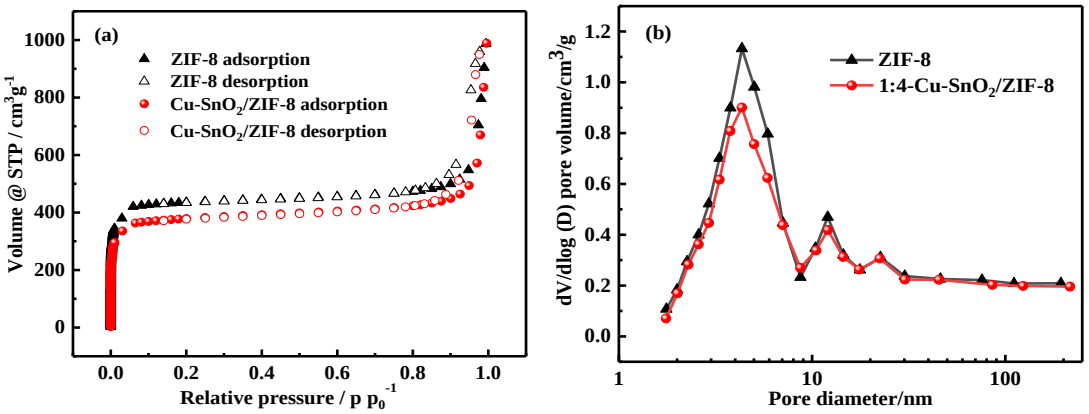

Figure 5. (a) N_2 adsorption-desorption isotherms; (b) Pore size distributions of 1:4-Cu-SnO_2/ZIF-8 composites.

The N_2 adsorption–desorption isotherms (Fig. 5a) of ZIF-8 and Cu-SnO_2/ZIF-8 belong to class IV adsorption isotherms with H type hysteretic loop, which is caused by capillary condensation at relatively high pressure and indicates that the aggregated nanoparticles produced fissure-like pores[33]. The pore diameters of the two materials are mainly in the range of 4–5 nm, and the abundant mesopores are attributed to the high specific surface area of ZIF-8 and composite materials. ZIF-8 possesses a BET surface area of 1319.07 $m^2 \cdot g^{-1}$. After being compounded with Cu-SnO_2, the BET surface area of Cu-SnO_2/ZIF-8 was 1153.05 $m^2 \cdot g^{-1}$, indicating that the spatial structure of ZIF-8 was not destroyed. The slight decrease in specific surface area may be due to Cu-SnO_2 occupying the pores of ZIF-8. However, Cu-SnO_2/ZIF-8 still maintained the original porous structure, which can absorb a large amount of CO_2

gas, promote electron transfer, inhibit the recombination of photoelectrons and hole pairs, and expose additional active sites to catalyze CO_2 conversion.

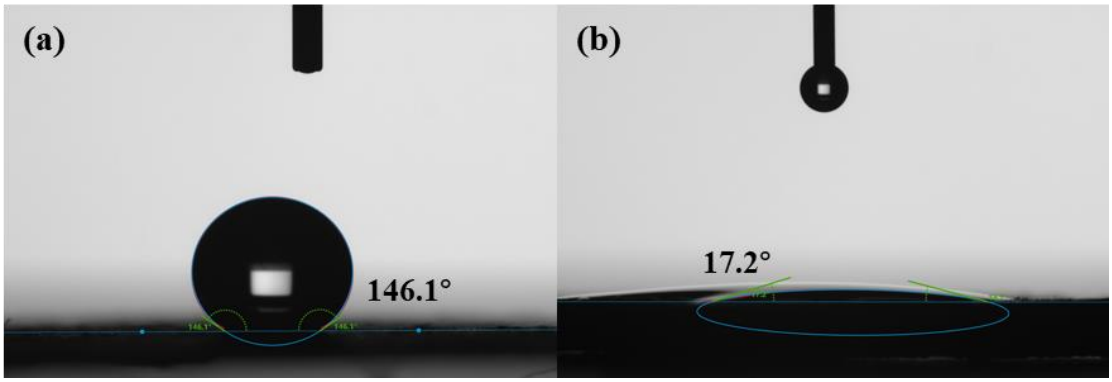

Figure 6. Photographs of water droplet that placed on the ZIF-8 (a) and Cu-SnO_2 (b).

The water contact angle (CA) of ZIF-8 is 146.1°, indicating that ZIF-8 is superhydrophobic(Fig.6a). Cu-SnO_2 shows excellent hydrophilicity with CA of 17.2° (Fig.6b). These results show that water could moisten Cu-SnO_2 but cannot penetrate further into ZIF-8 in the photoelectric catalytic reaction.

For the traditional diphase system, the surface of photoelectrocatalyst (solid phase) is completely covered by electrolyte (liquid phase), and the gaseous CO_2 cannot be in direct contact with the catalyst surface. Therefore, only the dissolved CO_2 can be utilized in diphase system, which is restricted by the poor solubility and slow diffusion rate of CO_2 in water. A hydrophilic–hydrophobic catalyst can solve this problem. A microscopic three-phase interface is formed at the contact surface between the catalyst and the electrolyte (as shown in Scheme.1). The hydrophobic ZIF-8 can directly capture the CO_2 bubbles in the electrolyte and transfer them to the photoelectric catalytic reaction interface. In addition, the hydrophilic and hydrophobic structures can effectively slow down the contact between the catalyst and water molecules, thereby effectively inhibiting the competitive HER and matching the proton generation rate with the activation rate of CO_2.

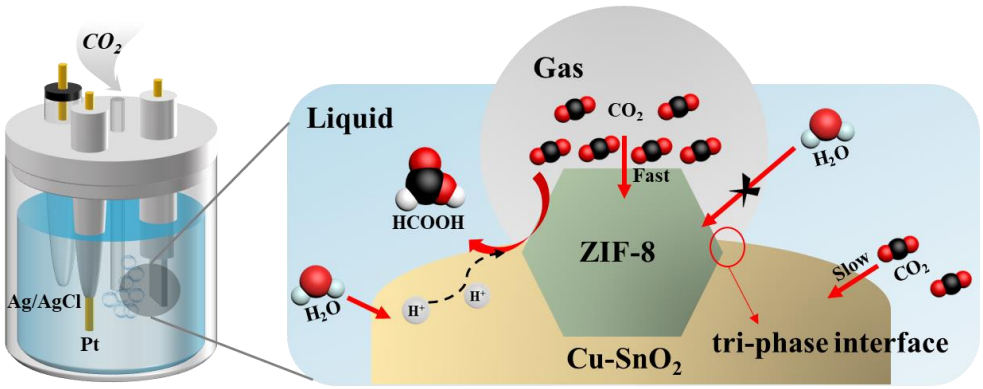

Scheme 1. Schematic illustration of thetri-phase photoelectrocatalytic system

3.2 Electrocatalytic Performance for CO_2 Reduction

Figure 7a shows the CV curves of Cu-SnO_2/ZIF-8 in N_2 or CO_2 saturated electrolyte. Compared with that in N_2, the Cu-SnO_2/ZIF-8 catalyst in CO_2 atmosphere showed higher current density in the applied potential range. In particular, the current density suddenly increased from -1.1 V, which is mainly caused by the combined action of HER and electrochemical CO_2 reduction. The increased current density in CO_2 atmosphere was generated by CO_2 reduction and further verifies the CO_2 electrocatalytic activity of the Cu-SnO_2/ZIF-8 catalyst. In addition, the appearance of an anode peak between -0.8 V and -1 V and a cathodic peak between -0.6 V and -0.8 V is due to the formation and reduction of Tin oxides[34].

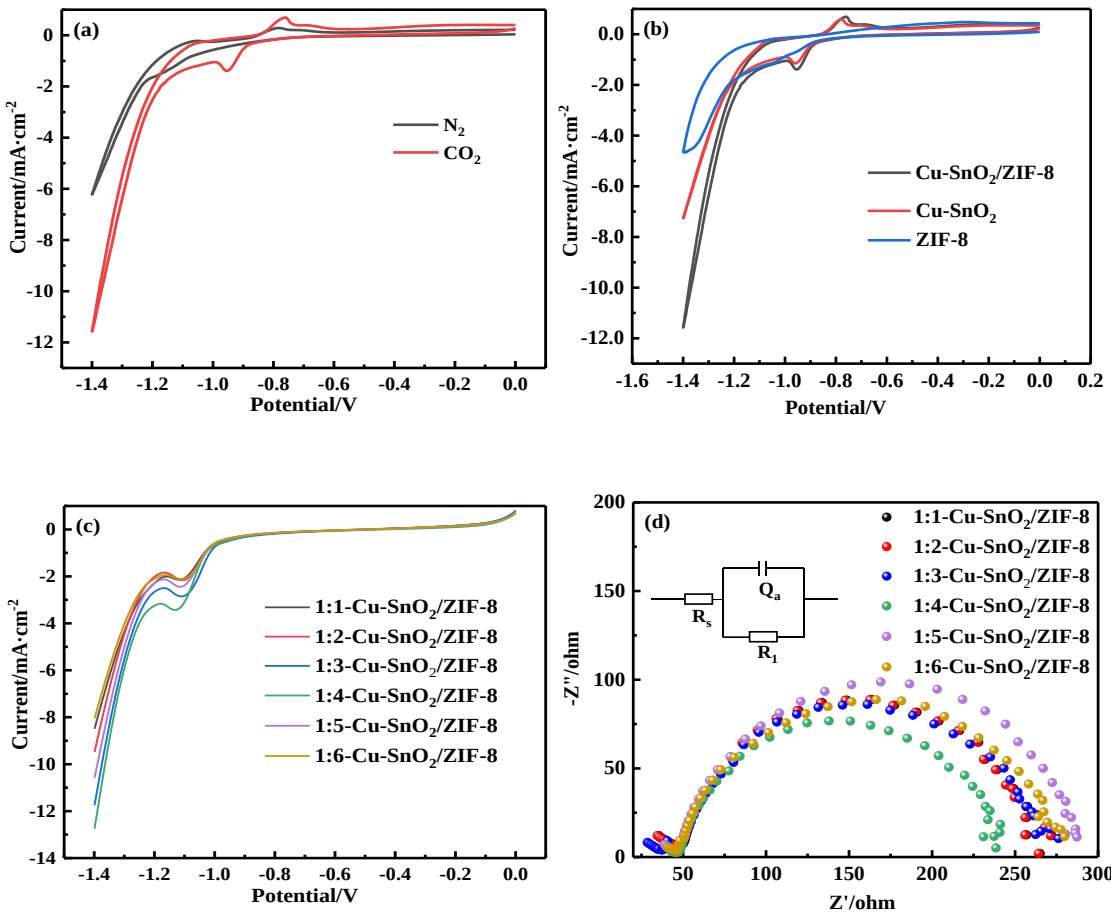

Figure 7. (a) CV curves of 1:4-Cu-SnO_2/ZIF-8 in N_2 or CO_2 saturated electrolyte; (b) CV curves of Cu-SnO_2, ZIF-8 and Cu-SnO_2/ZIF-8; (c) LSV curves of 1:x-Cu-SnO_2/ZIF-8 in CO_2 saturated electrolyte; (d) EIS spectroscopy of 1:x-Cu-SnO_2/ZIF-8.

In Fig.7b, Cu-SnO_2/ZIF-8 exhibits maximum current density due the synergistic effect between Cu-SnO_2 and ZIF-8 that promotes the electron transfer on the catalyst and the dissociation of $CO_2^{\bullet-}$ intermediate. In Fig.7c, 1:4-Cu-SnO_2/ZIF-8 catalyst shows the maximum current density of -12.8mA·cm^{-2}, which indicates its greatest electrocatalytic performance for CO_2. EIS spectroscopy was conducted and is shown in Fig.7d to further evaluate the electron transport efficiency. The catalyst with

a composite ratio of 1:4 presented the smallest impedance arc and therefore has the lowest electron transfer impedance and the fastest charge transfer velocity. Equivalent circuit fitting was performed for EIS impedance spectrum, where Rs is the solution internal resistance, R1 is the charge transfer internal resistance, C is the capacitance, and Q is the capacitance value. Calculation results are shown in Table 1. The 1:4-Cu-SnO_2/ZIF-8 exhibited the lowest diffusion resistance of 176.2 Ω, suggesting its fastest ion diffusion rate.

Table 1. Calculation results of EIS fitting circuit.

	R_s(Ω)	Qa	R_1(Ω)
1:1-Cu-SnO_2/ZIF-8	73.08	1.913×10^{-5}	201.5
1:2-Cu-SnO_2/ZIF-8	21.31	1.726×10^{-5}	223.0
1:3-Cu-SnO_2/ZIF-8	50.45	1.709×10^{-5}	204.0
1:4-Cu-SnO_2/ZIF-8	22.04	1.973×10^{-5}	176.2
1:5-Cu-SnO_2/ZIF-8	46.92	1.826×10^{-5}	222.9
1:6-Cu-SnO_2/ZIF-8	32.07	1.742×10^{-5}	206.9

3.3 Photocatalytic Performance for CO_2 Reduction

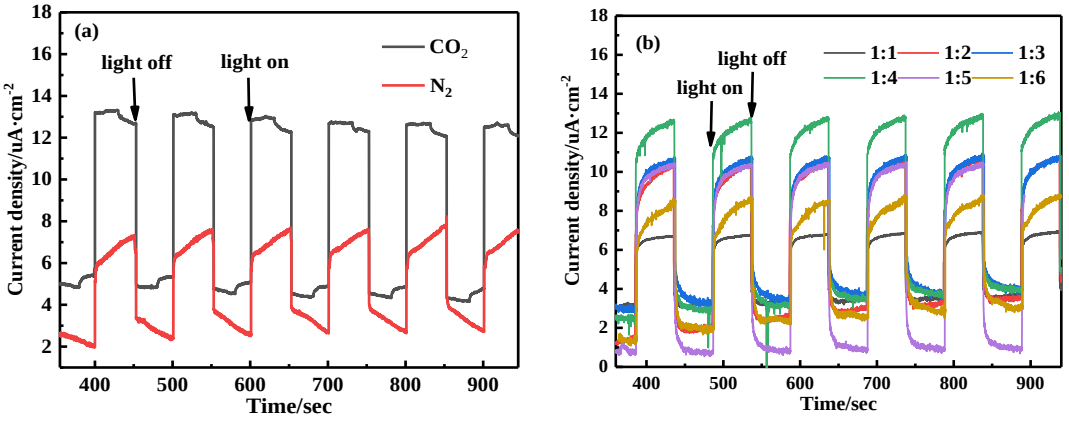

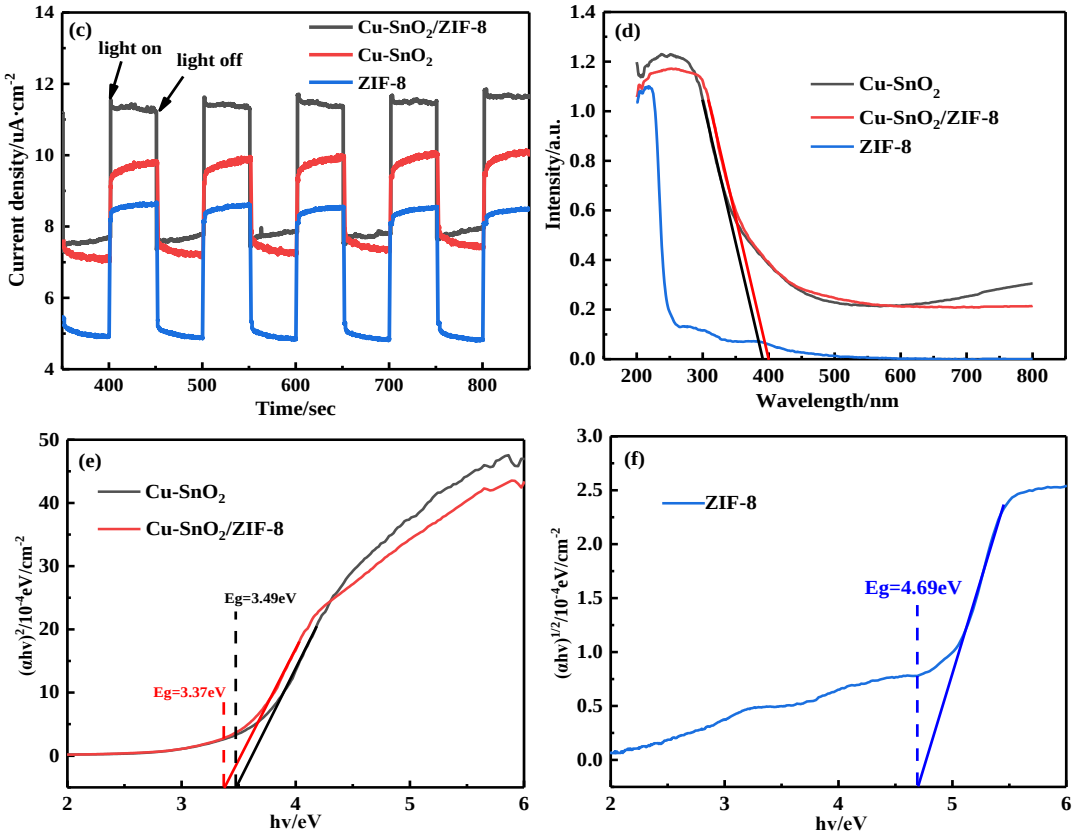

Figure 8. (a) Transient photocurrent responses of 1:4-Cu-SnO_2/ZIF-8 in CO_2 and N_2, (b) Transient photocurrent responses of 1: x-Cu-SnO_2/ZIF-8, (c) Transient photocurrent responses of Cu-SnO_2, ZIF-8 and Cu-SnO_2/ZIF-8 catalyst , (d) UV-vis spectra of pure ZIF-8, Cu-SnO_2 and Cu-SnO_2/ZIF-8 catalyst and estimated band gap of Cu-SnO_2, Cu-SnO_2/ZIF-8 and pure ZIF-8 (e, f)

Transient photocurrent responses curves under visible light and the UV-vis diffuse reflectance spectroscopy (DRS) were used to further investigate the photochemical activity of the prepared catalyst. The current density of the Cu-SnO_2/ZIF-8 in the CO_2 was significantly higher than that in N_2 (Fig.8a), indicating that CO_2 photoreduction could occurred under visible light. Figure 8b shows that the photocurrent density of 1:4-Cu-SnO_2/ZIF-8 was higher than that of catalysts with other ratios. This phenomenon may be attributed to the excess ZIF-8 in the composite that may increase the probability of collision between excited electrons and holes (e^-/h^+), thus promoting the recombination of photogenerated e^-/h^+ pairs[35]. Cu-SnO_2, ZIF-8, and Cu-SnO_2/ZIF-8 photoelectrocatalysts were also evaluated for comparison. As shown in Fig. 8c, the photocurrent density of Cu-SnO_2/ZIF-8 was higher than those of Cu-SnO_2 and pure ZIF-8. ZIF-8 can rapidly transfer photogenerated electrons in Cu-SnO_2 and react with the gaseous CO_2 adsorbed by itself, thus effectively inhibiting the recombination of photogenerated electrons and holes. Possible reasons were further explored from the UV-vis spectra. Figure 8d shows that ZIF-8 only absorbs ultraviolet light, and Cu-SnO_2 and Cu-SnO_2/ZIF-8 can absorb visible light between 200 and 800 nm. The band gap value can be obtained by Kubelka–Munk theorem (Eq (3))[36]. According to Tauc plots, the band gaps of Cu-SnO_2 and Cu-SnO_2/ZIF-8 were 3.49 and 3.37eV, respectively. ZIF-8 crystal has a certain influence on the band structure of Cu-SnO_2

nanoparticles, thus constituting a weak bond between the organic ligand (2-MI) and Sn^{4+} and resulting in the inhibition of interfacial charge recombination, shrinking of the band gap, and generation of sub-levels[37]. Figure 8f displays that the indirect band gap (n=2) of ZIF-8 is 4.69 eV, implying that pure ZIF-8 has a weak light catching property.

According to Eq. (6), the CB side potentials of Cu-SnO_2 and ZIF-8 were 0.25 and -0.86e V (vs. NHE)[38,39], respectively, and their E_g values were 3.49 and 4.69 eV, respectively. Therefore, the relative positions of the VB side of Cu-SnO_2 and ZIF-8 calculated by Eq(7) were 3.74 and 3.83 eV (vs. NHE), respectively. This result indicates that Cu-SnO_2 and ZIF-8 form an embedded heterojunction structure, and the electrons move from the CB of ZIF-8 to the CB of Cu-SnO_2, thus promoting the capture of electrons by the $HCOO^{\cdot}$ intermediate to generate formate.

3.4 Possible photoelectrocatalytic mechanism of CO_2

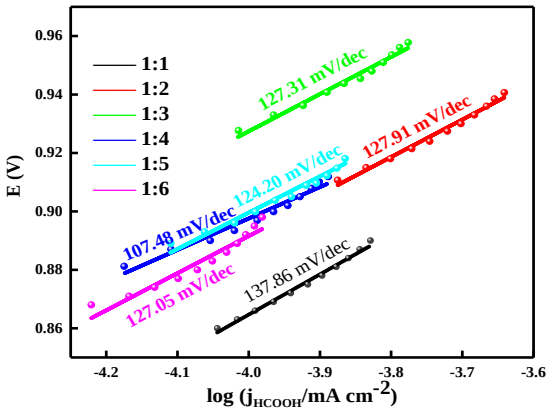

Figure 9. Tafel plots of HCOOH for 1:x-Cu-SnO_2/ZIF-8 catalysts.

Tafel plots of the samples are depicted in Fig.9 to further investigate the reaction mechanisms. According to Eq (4), the slopes of Tafel were 137.86, 127.91, 127.31, 107.48, 124.20, and 127.05 $mV{\cdot}dec^{-1}$. All of which are close to 118 $mV{\cdot}dec^{-1}$, indicating that the formation of the $CO_2^{\cdot-}$ intermediate by initial electron transfer is the rate determining step (RDS)[40,41]. Furthermore, 1:4-Cu-SnO_2/ZIF-8 possessed the smallest Tafel slope, indicating its fast electron transfer rate. The electrode reaction mechanism was determined by Butler–Volmer Eq.(5). A possible mechanism of CO_2 photoelectrocatalytic reduction system was proposed (scheme 2). Upon visible light irradiation, the electron–hole pairs are generated on the Cu-SnO_2 semiconductor. Electrons induced by visible light and electrons excited by applied voltage migrate to the CB of Cu-SnO_2 under the action of external electric field and then interact with CO_2 molecules adsorbed by ZIF-8 to reduce CO_2 to $CO_2^{\cdot-}$. $CO_2^{\cdot-}$ intermediate then reacts with the HCO_3^- in the electrolytic cell to form $HCOO^{\bullet}$. Finally, the $HCOO^{\bullet}$ in a highly excited state rapidly captures the electrons to generate the formate and desorbs it from the catalyst. The possible courses to convert CO_2 to formate using the Sn-based catalyst are presented as Eqs. (9–13)[42].

$$CO_2(air) \rightarrow CO_2(sds) \quad (9)$$

$$CO_2(ads) + e^- \rightarrow CO_2^{\bullet-} \quad (10)$$

$$CO_2^{\bullet-}(ads) + HCO_3^- \rightarrow HCOO^{\bullet}(ads) + CO_3^{2-} \quad (11)$$

$$HCOO^{\bullet}(ads) + e^- \rightarrow HCOO^-(ads) \quad (12)$$

$$HCOO^-(ads) \rightarrow HCOO^-(solution) \quad (13)$$

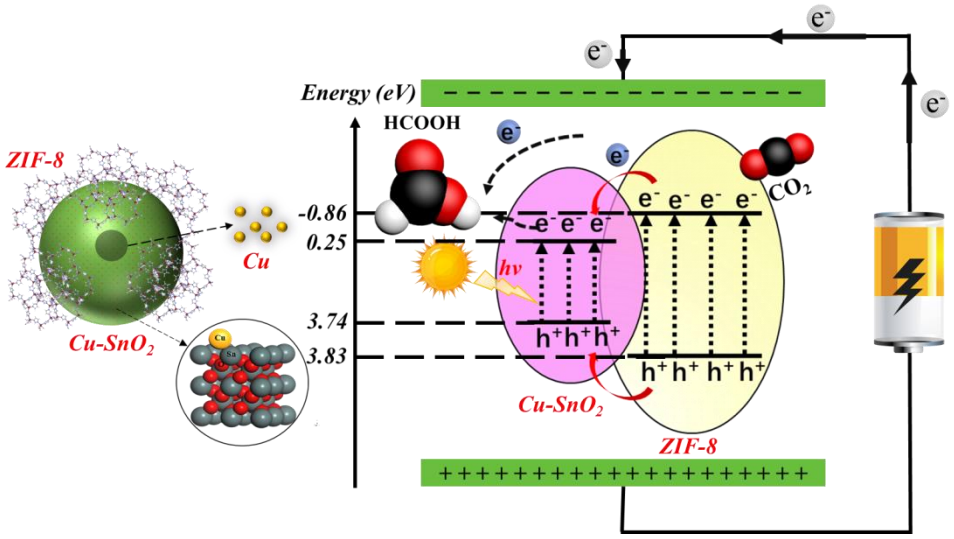

Scheme 2. Possible reaction mechanisms for photoelectric conversion of CO_2 on Cu-SnO_2/ZIF-8 catalyst

3.5 Faradaic Efficiency of Formate

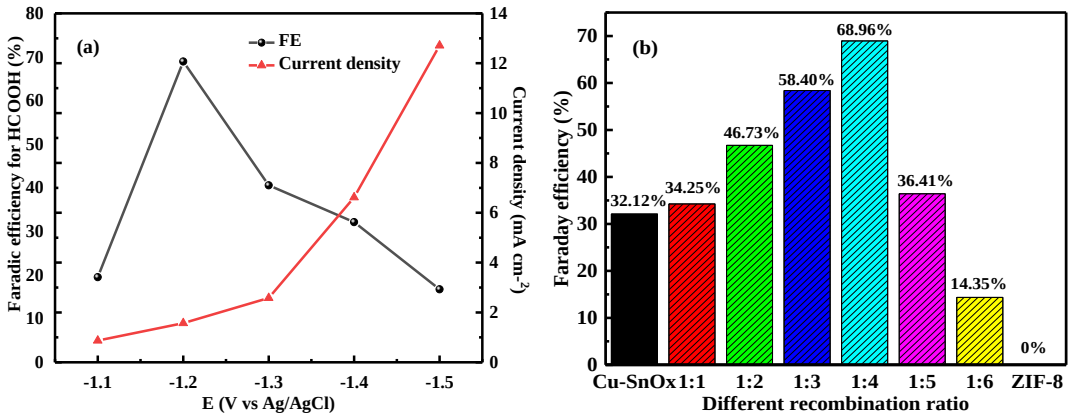

Figure 10. (a)The FE of HCOOH and current density at various potentials of 1:4-Cu-SnO_2/ZIF-8; (b) The FE of HCOOH of 1:x-Cu-SnO_2/ZIF-8 catalyst under illumination at 1.2 V;

A solution of 0.5M $NaHCO_3$ (pH=7.2) filled with CO_2 was electrolyzed for 4 h at a constant potential point (ranging from -1.1 V to -1.5 V vs. Ag/AgCl) and then subjected to 1H NMR spectral quantitative analysis to further determine the product selectivity of CO_2RR. The main product was formate. The FE at different voltages was calculated according to Eq. (9)[43,44], and the current density

and FE graphs at different voltages were plotted (Fig.10a). When the electrolysis voltage increased, the current density gradually increased, but the FE reached a maximum at -1.2 V. According to the conversion formula for Ag/AgCl electrode to reversible hydrogen electrode (Eq (1))[45] and reversible hydrogen electrode potential for conversion of CO_2 to formate (Eq (2))[24], the overpotential was as low as ~364 mV.

Catalyst-modified electrodes of different proportions were used for constant voltage electrolysis at the optimal electrolysis potential of -1.2 V. As shown in Fig.10b, FE increased after Cu-SnO_2 and ZIF-8 recombination, and the 1:4-Cu-SnO_2/ZIF-8 catalyst showed the highest FE of 68.96% in photoelectrocatalysis systems. The increase in FE may be attributed to following reasons: (1) the three-phase interface structure composed of hydrophobic ZIF-8 and hydrophilic Cu-SnO_2 can fully utilize and activate gaseous CO_2 molecules and directly transfer CO_2 from the gas phase to the photoelectric catalytic reaction interface to achieve efficient photoelectric catalytic reaction; (2) ZIF-8 has excellent CO_2 adsorption performance and the ability to increase the electrocatalytic active area of the electrode; (3) the introduction of SnO_2 enhanced the intrinsic conductivity of ZIF-8 and accelerated the electron transfer rate; and (4) Sn is an important active site for the generation of formates and could be fully dispersed and exposed by attaching to ZIF-8. With excellent atomic hydrogen storage and transfer performance, ZIF-8 can rapidly transfer the protons produced in the hydrophilic layer and prevent the formation of H_2, thus effectively inhibiting the competitive HER. As a consequence, formate can be formed rapidly and selectively under low overpotential.

3.6 Stability test

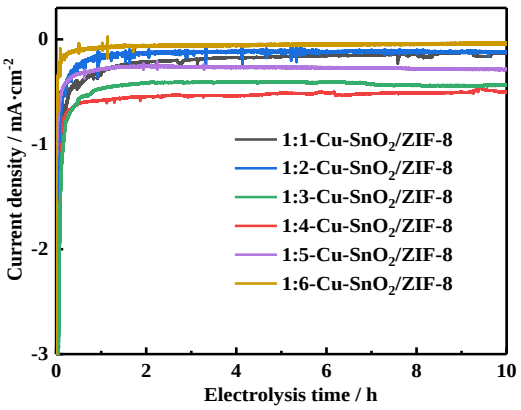

Figure 11. Electrolysis stability of 1:x-Cu-SnO_2/ZIF-8 at -1.0 V vs. Ag/AgCl over a 10 h period.

Catalyst stability frequently restricts its practical application. Hence, a 10 h chronoamperometry experiment at a potential of -1.0 V was conducted to evaluate the stability of 1:x-Cu-SnO_2/ZIF-8 in CO_2 atmosphere. As shown in Fig.11, the current density decreased sharply at the beginning of the experiment and then stabilized possibly due to the production of intermediate products in the initial stages of the

experiment[43]. With time, the current density of the catalyst did not show substantial attenuation during 10 h, indicating its excellent stability.

4. CONCLUSIONS

A novel Cu-SnO_2/ZIF-8 hydrophilic-hydrophobic composite catalyst was synthesized successfully by simple in situ synthesis and showed excellent catalytic performance for CO_2 photoelectric conversion. The 1:4-Cu-SnO_2/ZIF-8 composite revealed the best catalytic conversion performance with a BET surface area of 1153.05 $m^2 \cdot g^{-1}$. The FE of formate reached 68.96%, the overpotential was as low as ~364 mV, and the maximum current density was close to 12.8 $mA \cdot cm^{-2}$ at -1.4V vs. Ag/AgCl. The band gap of the composite material narrowed from 3.49 eV to 3.37 eV compared with that of Cu-SnO_2, indicating that much visible light can be absorbed, and additional photogenic carriers can be generated. In addition, its 10 h stability was feasible in practical applications. This excellent performance may be attributed to the three-phase interface structure that can directly transport CO_2 to the photoelectrocatalytic reaction interface, thus replacing the diffused CO_2 in the liquid phase. ZIF-8 with super specific surface area contributed additional active sites, which greatly promoted the conversion of CO_2 to formate. This study provides a new idea of developing catalysts for photoelectrocatalytic CO_2 reduction system.

ACKNOWLEDGEMENTS
This work is funded by the National Natural Science Foundation of China (Grant No. 51703151), the Natural Science Foundation of Shanxi Province (Grant No. 201601D011023) and Science and Technology Innovation Project of Shanxi Province Colleges and Universities (Grant No. 2020L0068). The authors sincerely thanks for anonymous reviewers for their valuable comments.

References

1. B. Kumar, M. Asadi, D. Pisasale, S. Sinha-Ray, B.A. Rosen, R. Haasch, J. Abiade, A.L. Yarin, A. Salehi-Khojin, *Nat. Commun.*, 4 (2013) 1–8.
2. M. Marszewski, S. Cao, J. Yu, M. Jaroniec, *Mater. Horizons*, 2 (2015) 261–278.
3. N. Zhang, R. Long, C. Gao, Y. Xiong, *Sci. China Mater.*, 61 (2018) 771–805.
4. Y. Xu, J. Mo, G. Xie, X. Wang, S. Ding, *J. Mater. Chem. A*, 8 (2020) 4457–4463.
5. Z. Pan, E. Han, J. Zheng, J. Lu, X. Wang, Y. Yin, G.I.N. Waterhouse, X. Wang, P. Li, *Nano-Micro Lett.*, 12 (2020).
6. H.K. Lee, C.S.L. Koh, Y.H. Lee, C. Liu, I.Y. Phang, X. Han, C.K. Tsung, X.Y. Ling, *Sci. Adv.*, 4 (2018) 1–9.
7. Z. Zhang, S. Xian, H. Xi, H. Wang, Z. Li, *Chem. Eng. Sci.*, 66 (2011) 4878–4888.
8. Y. Wang, P. Hou, Z. Wang, P. Kang, *ChemPhysChem*, 18 (2017) 3142–3147.
9. Q. Liu, Z.X. Low, L. Li, A. Razmjou, K. Wang, J. Yao, H. Wang, *J. Mater. Chem. A*, 1 (2013) 11563–11569.
10. S. Zhao, Y. Wang, J. Dong, C.T. He, H. Yin, P. An, K. Zhao, X. Zhang, C. Gao, L. Zhang, J. Lv, J. Wang, J. Zhang, A.M. Khattak, N.A. Khan, Z. Wei, J. Zhang, S. Liu, H. Zhao, Z. Tang, *Nat. Energy*, 1 (2016) 1–10.

11. X. Zu, X. Li, W. Liu, Y. Sun, J. Xu, T. Yao, W. Yan, S. Gao, C. Wang, S. Wei, Y. Xie, *Adv. Mater.*, 31 (2019) 1–8.
12. L. Zhang, R. Tong, W. Ge, R. Guo, S.E. Shirsath, J. Zhu, *J. Alloys Compd.*, 814 (2020) 152266.
13. X. Hu, N. Wang, Y. Hao, Z. Xu, M. Wang, G. Shi, H. Yang, Z. Liang, *Chem. J. Chinese Univ.*, 39 (2018) 2265–2271.
14. G. Zhan, H.C. Zeng, *Nat. Commun.*, 9 (2018) 1–12.
15. X. Wang, J. Lv, J. Zhang, X.L. Wang, C. Xue, G. Bian, D. Li, Y. Wang, T. Wu, *Nanoscale*, 12 (2020) 772–784.
16. K.S. Park, Z. Ni, A.P. Côté, J.Y. Choi, R. Huang, F.J. Uribe-Romo, H.K. Chae, M. O'Keeffe, O.M. Yaghi, *Proc. Natl. Acad. Sci. U. S. A.*, 103 (2006) 10186–10191.
17. Q. Bao, Y. Lou, T. Xing, J. Chen, *Inorg. Chem. Commun.*, 37 (2013) 170–173.
18. Y. Pan, Y. Liu, G. Zeng, L. Zhao, Z. Lai, *Chem. Commun.*, 47 (2011) 2071–2073.
19. Y. Ban, Z. Li, Y. Li, Y. Peng, H. Jin, W. Jiao, A. Guo, P. Wang, Q. Yang, C. Zhong, W. Yang, *Angew. Chemie - Int. Ed.*, 54 (2015) 15483–15487.
20. K.Y.A. Lin, H.A. Chang, *Water. Air. Soil Pollut.*, 226 (2015).
21. Y. Hu, Z. Liu, J. Xu, Y. Huang, Y. Song, *J. Am. Chem. Soc.*, 135 (2013) 9287–9290.
22. Y. Wang, Y. Xu, H. Ma, R. Xu, H. Liu, D. Li, Z. Tian, *Microporous Mesoporous Mater.*, 195 (2014) 50–59.
23. T. Krishnakumar, N. Pinna, K.P. Kumari, K. Perumal, R. Jayaprakash, *Mater. Lett.*, 62 (2008) 3437–3440.
24. Y. Li, H. Yang, X. Hu, H. Tian, M. Gao, D. Zhang, Z. Li, D. Yang, *ChemElectroChem*, 6 (2019) 3782–3790.
25. J. Zhou, J. Lian, L. Hou, J. Zhang, H. Gou, M. Xia, Y. Zhao, T.A. Strobel, L. Tao, F. Gao, *Nat. Commun.*, 6 (2015).
26. D. Hulicova-Jurcakova, M. Seredych, G.Q. Lu, T.J. Bandosz, *Adv. Funct. Mater.*, 19 (2009) 438–447.
27. F. Sun, J. Wang, H. Chen, W. Li, W. Qiao, D. Long, L. Ling, *ACS Appl. Mater. Interfaces*, 5 (2013) 5630–5638.
28. Y. Xiao, P. Sun, M. Cao, *ACS Nano*, 8 (2014) 7846–7857.
29. Z. Hu, D. Zhao, *CrystEngComm*, 19 (2017) 4066–4081.
30. Q. Li, J. Fu, W. Zhu, Z. Chen, B. Shen, L. Wu, Z. Xi, T. Wang, G. Lu, J.J. Zhu, S. Sun, *J. Am. Chem. Soc.*, 139 (2017) 4290–4293.
31. M. Punginsang, A. Wisitsoraat, C. Sriprachuabwong, D. Phokharatkul, A. Tuantranont, S. Phanichphant, C. Liewhiran, *Appl. Surf. Sci.*, 425 (2017) 351–366.
32. L. Li, F. Cai, F. Qi, D.K. Ma, *J. Alloys Compd.*, 841 (2020) 1–8.
33. M. Zhou, S. Wang, P. Yang, C. Huang, X. Wang, *ACS Catal.*, 8 (2018) 4928–4936.
34. M. Asadi, B. Kumar, A. Behranginia, B.A. Rosen, A. Baskin, N. Repnin, D. Pisasale, P. Phillips, W. Zhu, R. Haasch, R.F. Klie, P. Král, J. Abiade, A. Salehi-Khojin, *Nat. Commun.*, 5 (2014) 1–8.
35. X. Zeng, L. Huang, C. Wang, J. Wang, J. Li, X. Luo, *ACS Appl. Mater. Interfaces*, 8 (2016) 20274–20282.
36. B.S. Lee, J.R. Abelson, S.G. Bishop, D.H. Kang, B.K. Cheong, K.B. Kim, *J. Appl. Phys.*, 97 (2005).
37. Y. Li, A. Pang, C. Wang, M. Wei, *J. Mater. Chem.*, 21 (2011) 17259–17264.
38. S. Dursun, İ.C. Kaya, M. Kocabaş, H. Akyildiz, V. Kalem, *Int. J. Appl. Ceram. Technol.*, 17 (2020) 1479–1489.
39. J. He, J. Ye, Y. Zhang, L. Kong, X. Zhou, Y. Ma, Y. Yang, *ChemistrySelect*, 5 (2020) 3746–3755.
40. S. Zhang, P. Kang, T.J. Meyer, *J. Am. Chem. Soc.*, 136 (2014) 1734–1737.

41. D.H. Won, C.H. Choi, J. Chung, M.W. Chung, E.H. Kim, S.I. Woo, *ChemSusChem*, 8 (2015) 3092–3098.
42. Q. Zhao, T. Wang, Y. Miao, F. Ma, Y. Xie, X. Ma, Y. Gu, J. Li, J. He, B. Chen, S. Xi, L. Xu, H. Zhen, Z. Yin, J. Li, J. Ren, W. Jie, *Phys. Chem. Chem. Phys.*, 18 (2016) 18719–18726.
43. X. Hu, H. Yang, M. Guo, M. Gao, E. Zhang, H. Tian, Z. Liang, X. Liu, *ChemElectroChem*, 5 (2018) 1330–1335.
44. Y.H. Lee, Y.S. Kim, H.C. Lee, S.W. Lee, Y.N. Kang, J.H. Kang, S.H. Hong, Y.K. Kim, S.J. Kim, M.I. Ahn, D.H. Han, I.R. Yoo, J.G. Park, S.W. Sung, K.Y. Lee, *Br. J. Radiol.*, 88 (2015).
45. S. Kim, W.J. Dong, S. Gim, W. Sohn, J.Y. Park, C.J. Yoo, H.W. Jang, J.L. Lee, *Nano Energy*, 39 (2017) 44–52.